Porous silica derived from sago waste and its application for the preparation of SiO₂/C composites as air cathodes for primary aluminum-air batteries

H. Aripin[1,], Sutisna Sutisna[1], Edvin Priatna[1], I Nyoman Sudiana[2], Endang Surahman[3], Svilen Sabchevski[4]*

[1] Department of Electrical Engineering, Faculty of Engineering, Siliwangi University, Tasikmalaya 46115, Indonesia.
[2] Department of Physics, Faculty of Mathematics and Natural Science, Haluoleo University, Kendari, Indonesia.
[3] Department of Physics Education, Faculty of Education and Teacher Training, Siliwangi University, Tasikmalaya 46115, Indonesia.
[4] Lab. Plasma Physics and Engineering, Institute of Electronics of the Bulgarian Academy of Sciences, 72 Tzarigradsko Shose Blvd., Sofia 1784, Bulgaria.
[*]E-mail: aripin@unsil.ac.id

In the present study, a porous air cathode made of amorphous silica xerogel (a-SX) derived from sago waste was investigated for treating the first discharge of an aluminum-air (Al-air) battery. Four types of air cathode samples were produced by varying the content of polyvinylidene fluoride (PVDF) binder from 5 wt % to 30 wt % in a composite of a-SX, carbon black (C), and PVDF. The detailed structural characterization of the explored composite samples was performed using various techniques, such as X-ray diffraction (XRD), Fourier transform infrared (FTIR) spectroscopy, scanning electron microscopy (SEM), and N_2 adsorption-desorption isotherms. The performance of the prepared air cathode in the Al-air battery was tested successfully during the first discharging treatment. The study demonstrated that the volume fraction of the microporous structure in the air cathode sample increases with increasing binder content, while for mesoporous structures, it acts in the opposite direction. The sample containing a binder of 10 wt % provides the mesoporous structure with the largest volume fraction and the formation of discharge products with the smallest fraction in the mesopore, and their presence generates a discharge capacity in an Al-air battery with the longest stable plateau voltage.

1. INTRODUCTION

Silica (SiO_2) in all its allotropic forms is a material that is widely used for various applications in many industrial processes and electronic devices [1-3]. Among these applications are different advanced electrochemical energy storage and conversion devices with high power and energy density, such as fuel cells, supercapacitors, and batteries. The batteries are considered quite promising and actively studied devices that possess an attractive combination of features. Most notably, the batteries are characterized by theoretical energy densities in the range of 2-12 kWh/kg [4], nominal cell voltages of 1-3 V [5], and power densities of 1000-10000 W/kg. The batteries can deliver high capacity with high charge-discharge cycle durability [6], store full capacity when charged quickly [7], and retain at least 80% of their original capacity for a high number of charge cycles. Such favorable parameters for the storage and conversion of electrical energy are important for advanced technologies in today's society and are used in many application systems, such as hybrid electric vehicles, power backup systems for wind and solar energy, portable electronics, and uninterruptible power supplies.

One of the most promising and highly appreciated battery types is the metal-air battery, in particular the aluminum-air battery. The main advantages of an Al-air battery are as follows. First, these batteries use aluminum metal as an anode, which is low-cost, safe, and abundant. The costs of the cathode part are reduced because it uses freely available oxygen from ambient air as the cathode source. Second, technologically, the usage of oxygen leads to a significantly reduced battery weight and provides more free space for energy storage.

One of the important components in the structure of the Al-air battery is the air cathode, which is composed of an active layer, a cathode binder, and a conductive additive. The air cathode facilitates the oxygen reaction and is regarded as a key factor that determines the practical energy and power density of the batteries. However, the sluggish kinetics of the oxygen reaction on the air cathode hinders the development of Al-air batteries with high discharge capacity, making it necessary to combine the three components of the air cathode to obtain an appropriate electronic active layer of air cathodes in Al-air batteries.

SiO_2 has been successfully employed as an active layer material in various types of batteries, such as Li-ion [8], Zn-air [9], and Li-air batteries [10]. These results demonstrated that experimentally, the prepared SiO_2 inhibits a high charge transfer [11] due to its low characteristic conductivity of approximately 10^{-4} S/m and the volume change of particles during the electrochemical reaction. Such problems can be overcome by adding carbon black as a conductive additive. In several studies, the use of a carbon black of approximately 10 wt % to dope SiO_2 in Li-ion batteries [12, 13] demonstrates high reversible capacities, excellent cycling stability, and superior rate capabilities. However, in these batteries, agglomerates were found during preparation of the slurry for the active layer when a polyvinylidene fluoride (PVDF) binder was introduced into the SiO_2 composite. As a result, an unequal distribution of pores is observed in the agglomerates, thus causing the narrow size of micropores for the SiO_2 composite. In this case, oxygen diffusion and electrolyte access are limited toward the active site surface at the air cathode. In another study, polytetrafluoroethylene (PTFE) and guar gum (GG) were used as binders to provide sufficient electrochemical stability of the SiO_2 active layer in an Al-air battery, which results in a much slower charge transfer than using a PVDF binder [14, 15]. Therefore, PVDF is

the binder with the best stability; however, the idea of optimizing the PVDF binder content while maintaining the required properties and functionalities of the air cathode is essential.

In this paper, we report the results of an investigation on the preparation of air-cathode active layers based on a composite of SiO_2 in the form of silica xerogel and carbon black with various loadings of the PVDF binder. Furthermore, we also discuss the structural properties of the air cathode obtained using X-ray diffraction (XRD), Fourier transform infrared (FTIR) spectroscopy, scanning electron microscopy (SEM) and N_2 adsorption-desorption isotherms to obtain a better understanding of the effect of the PVDF binders on the discharging capacity of an Al-air battery.

2. EXPERIMENTATION

2.1. Preparing the raw material and air cathode sample

The a-SX was produced from the extracted solid residue of sago waste available at a community sago processing plant in Kendari, Indonesia. The procedures of the extraction have been described in detail, and the purity of a-SX was as high as 98.8% [16, 17]. The average particle size of the solid sago waste residue is 656 nm.

Table 1. Compositional formulations for the prepared air cathode sample.

Sample	Mass percentages (wt %)		
	a-SX	C	PVDF
S85	85	10	5
S80	80	10	10
S70	70	10	20
S60	60	10	30

The raw materials for the air cathode are a-SX, carbon black (C) and PVDF binder. C and PVDF powders are commercially available materials supplied by Sigma Aldrich. The composite powder for the air cathode was prepared by mixing a-SX, C, and a binder of PVDF. Table 1 presents the compositional formulations for the prepared air cathode samples. Based on a fixed C composition, the prepared chemical compositions of a-SX-PVDF were 60, 70, 80, and 85 wt % of a-SX in aqueous slurry. The S85 sample was prepared using 85 wt % a-SX powder and 10 wt % C powder. These materials were mixed and then pulverized for 24 hours at room temperature by an alumina ball mill. Approximately 5 wt % PVDF was mixed in 10 mL of N-methylpyrrolidone (NMP) solvent and then stirred using a magnetic stirrer to obtain a homogeneous binder suspension. The mixed powder of a-SX and C was dropped slowly into the PVDF solution and stirred to obtain a homogeneous stable slurry in the paste phase. The prepared slurry was deposited on the surface of a square nickel mesh substrate with an area of 16 cm^2. The layer thickness of 0.6 mm was adjusted using doctor blading. The deposited slurry was dried at 105 °C for 24 h in an oven. Making the S80, S70, and S60 samples was carried out following

the same steps as described above. The prepared samples were termed samples before receiving the discharging treatment.

2.2. Method for testing the Al-air battery

The Al-air battery cell is composed of an anode and a cathode with an active area of approximately 16 cm^2, as well as a polypropylene (PP) separator inserted between them. An aluminum (Al) plate of alloy 1100 was used as the anode material, and an active layer of the S85 sample was attached to the surface of the nickel mesh substrate as an air cathode. An aqueous solution of 6 M concentrated KOH was used as an electrolyte. Polypropylene is soaked in KOH solution to provide an effective transfer medium for hydroxide ion crossover. An Al plate at the anode and a nickel mesh at the cathode were used as the terminals for measurement based on electrochemical impedance spectroscopy (EIS) and cell discharge. The procedures for EIS measurements have been described in detail in previous studies [15]. Testing of the constant current discharging was carried out by using a multichannel battery testing system (BTS-MPTS, China) at a discharge current of 10 mA and a cutoff voltage of 0.05 V. Furthermore, referring to a sample of S85 after receiving the discharging treatment, it is termed an SD85 sample. The same procedure was carried out for the S80, S70, and S60 samples, and each of the samples was labeled SD80, SD70, and SD60, respectively.

2.3. Method for characterizing the air cathode sample

X-ray diffraction patterns for air cathode samples before and after discharge were obtained using a Smartlab X-ray diffractometer with a Cu Kα radiation wavelength of 0.15418 nm. The measured trace of the diffraction angle was in the range from 10 to 90 degrees. FTIR spectroscopy was carried out using a Varian 800 FTIR spectrometer in the wavenumber range from 400 to 4000 cm^{-1}. All FTIR measurements were carried out in specular reflectance mode using the KBr pellet technique at room temperature. Furthermore, the surface microstructure of the air cathode samples was characterized by a scanning electron microscope (SEM) JEOL JSM-6400 with a magnification of 7500 times. The distribution of pore sizes in the air cathode samples before discharge was evaluated by a nitrogen adsorption-desorption method using a Quantachrome Nova-1000 Analyzer.

3. RESULTS AND DISCUSSION

Figure 1a and 1b display the XRD patterns of the prepared air cathode before and after discharge, respectively. For the a-SX sample, one broad peak can be observed in the range of 20–22.51$^°$, which is characteristic of the presence of an a-SX. For the SX85 sample, the weak diffraction peaks of α-PVDF at 18.5$^°$ and β-PVDF at 19.9$^°$ overlap with a broad peak of a-SX [18]. As the PVDF binder content increases from 10 wt % (SX80) to 30 wt % (SX60), the peak intensities of α-PVDF and β-PVDF increase as well. Furthermore, the XRD peaks corresponding to carbon black were not found, probably due to the small (and therefore undetectable) amount. Compared to Figure 1a, Figure 1b shows that the additional

peaks at 22.3° and 40.2° are associated with a diffraction pattern of Al(OH)$_3$ [19], confirming that the discharge product of Al(OH)$_3$ was formed during the discharge stage. The detected peak of Al(OH)$_3$ was weak since its diffraction peaks coincided with the broad peak of a-SX. As shown in Figure 1b, the peak intensity of the broad diffraction pattern of a-SX is reduced, and its peak position shifts toward higher diffraction angles. In many studies, the intensity reduction and the shift of the broad diffraction pattern of a-SX were found to be induced by the presence of water molecules, which led to structural conformational changes in the silica network [20, 21]. In our case, during the discharging process, the discharge product of Al(OH)$_3$ accumulates at the air cathode and generates water molecules, and the structure of the silica network changes due to the increase in the water molecule content.
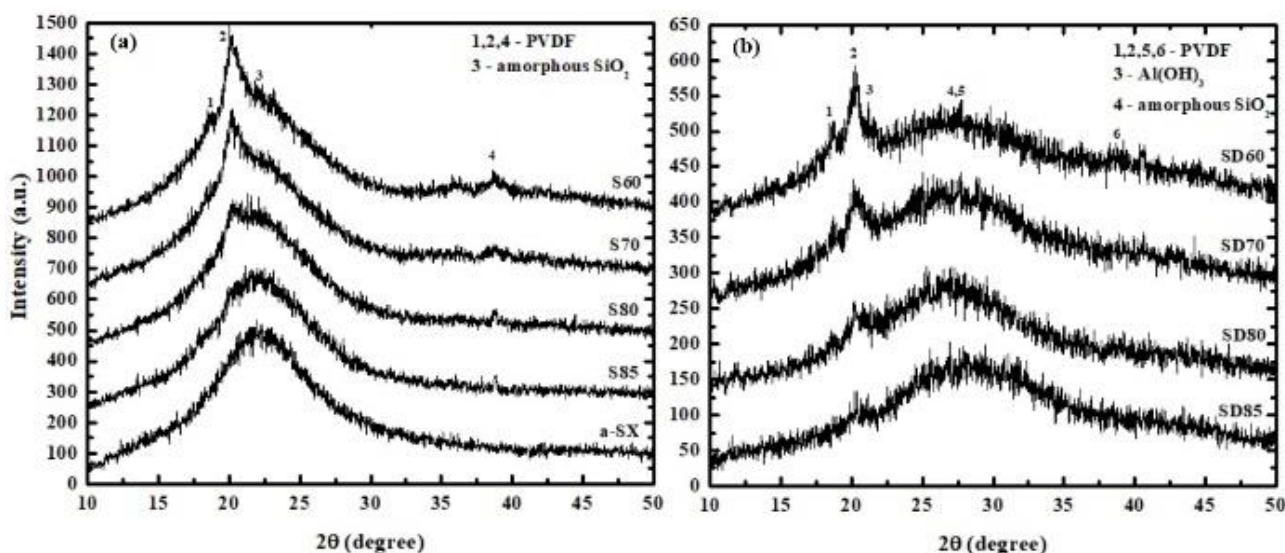
Figure 1. XRD pattern of the air cathode (a) before discharge and (b) after discharge.
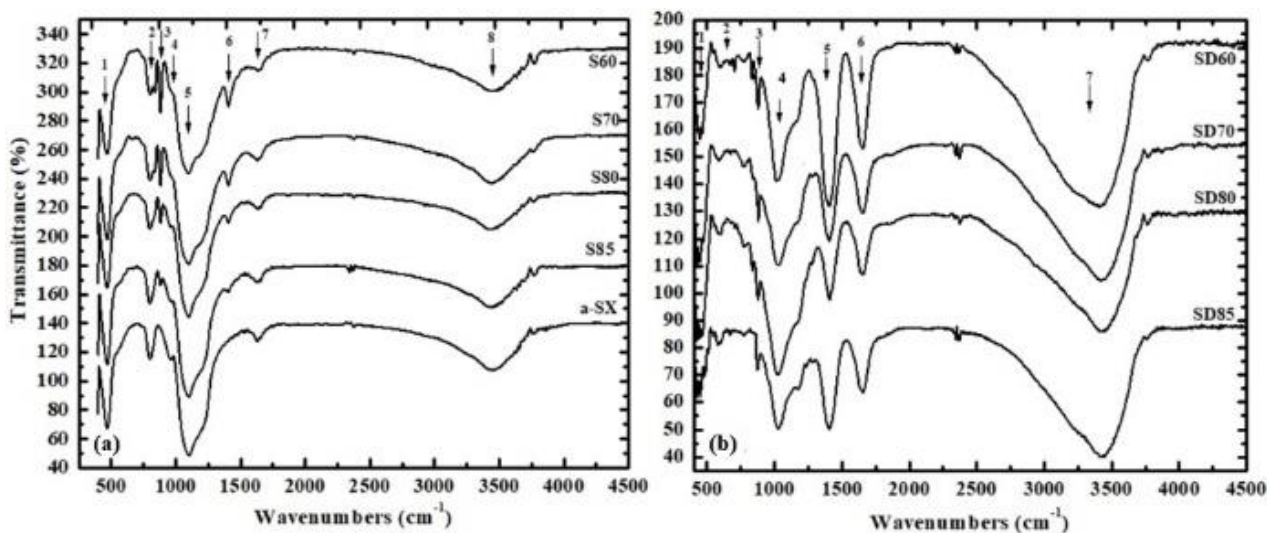

Figure 2. FTIR spectra for the air cathode (a) before discharge and (b) after discharge.

Figure 2a and 2b display FTIR spectra of the prepared air cathode before and after discharge, respectively. In Figure 2a, the spectrum of the a-SX sample shows peaks at 465 cm^{-1} (peak 1) and 1100 cm^{-1} (peak 5), relating to the Si–O–Si asymmetric vibration and bending vibrations, respectively [22].

Peak 2 at approximately 790 cm^{-1} and peak 4 at approximately 950 cm^{-1} are attributed to the Si-O-Si symmetric vibration and the Si-OH stretching band, respectively [23]. Peak 7 observed at 1620 cm^{-1} is assigned to the bending H–O–H bond groups of adsorbed water molecules, and peak 8 at approximately 3452 cm^{-1} can be attributed to -OH stretching of hydroxyl groups or the remaining water [24]. For the S85 sample, compared to the initial spectrum (a-SX sample), two additional peaks (peaks 3 and 6) can be observed. They correspond to the characteristic peaks of the amorphous phase in PVDF at 880 cm^{-1} [25] and the C–O stretching vibration of the carboxyl group at 1380 cm^{−1} [26]. The intensity of the peak absorbance for the functional groups PVDF and C-O increases as the PVDF content in the air cathode increases. Compared to Figure 2a and Figure 2b, the peak intensity associated with the Si-O-Si symmetric vibration is reduced, and the Si-OH stretching band disappears. Furthermore, the intensity of the discharged air cathode contains a sharp peak related to the -OH stretching mode. This peak is attributed to $Al(OH)_3$ due to the hydrogen bonded $Al(OH)_3$ hydroxyl groups or the structural water molecules present within $Al(OH)_3$ [27].

Figure 3 shows the integrated intensity for the -OH stretching mode at 3452 cm^{-1} of the air cathode sample before and after discharge with different content of the PVDF binder. The integrated intensity of the -OH stretching mode for the discharged air cathode sample is much higher than the integrated intensity of the -OH stretching mode of the air cathode sample before discharge. We assume that the discharged samples contain a larger number of structural water molecules bound in the sample, ascribed to the side reaction of oxygen reduction during the discharging process. This behavior is in line with the results of previous studies [28, 29]. Furthermore, the number of water molecules decreases with decreasing PVDF binder content from 30 wt % (SD60) to 10 wt % (SD80), and afterward, it increases as the binder content is lowered to 5 wt % (SD85).
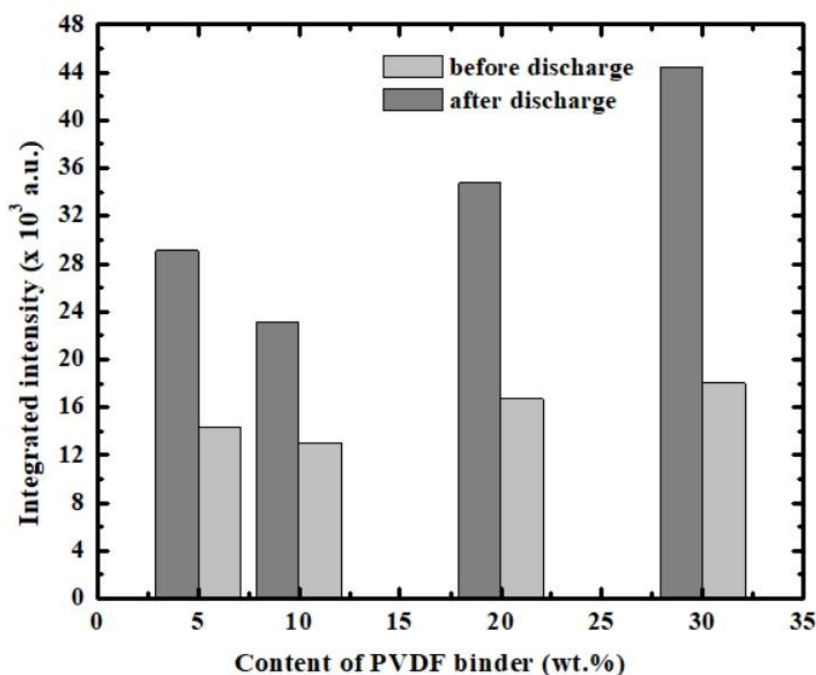
Figure 3. Integrated intensity for the -OH stretching mode at 3452 cm^{-1} of the air cathode before and after discharge with varying a-SX content.

Figure 4 presents SEM images of the prepared air cathode sample before and after discharge. For the air cathode sample before discharge, the S85 sample exhibits a rough and aggregated surface texture with large and inhomogeneous pores that are composed of stacked particles with a shape similar to the shape of the powder. The individual particles are not visible, and the aggregates have an irregular shape. The image of the S80 sample indicates the presence of a few smaller interconnected pores. The formation of pores is caused by bridging particles that have fairly loose bonds and are distributed homogeneously in the PVDF binder. Furthermore, the number of pores in the S80 sample was found to be more than the number of pores in the S85, and these pores were also relatively larger in size. The image of the S70 sample shows a surface with aggregated texture and reduced pore size. Furthermore, the S60 image is characterized by a denser microstructure accompanied by an aggregated surface. Overall, the reduction in the content of the PVDF binder results in a highly porous structure created from interconnected pores.
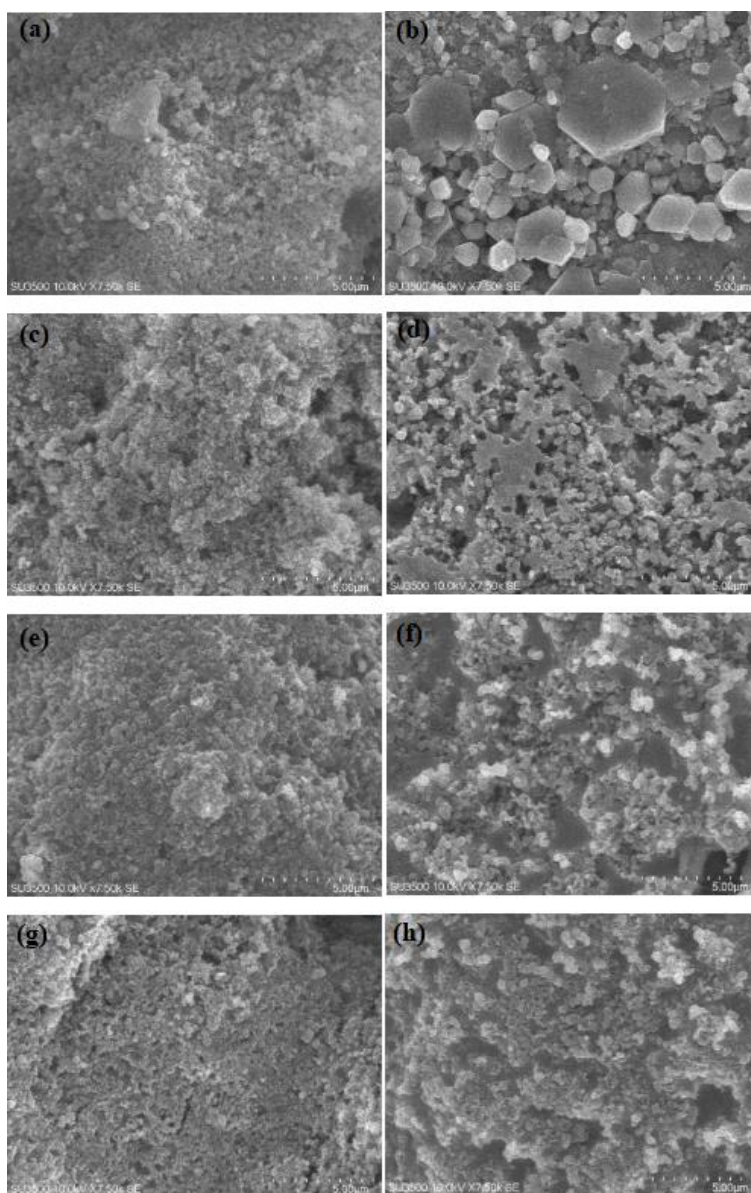
Figure 4. SEM images of the cathode before and after discharge of S85 (a) and SD85 (b), S80 (c) and SD80 (d), S70 (e) and SD70 (f), and S60 (g) and SD60 (h).

From this SEM observation, the cathode with PVDF content of 5 wt % (S85) and 10 wt % (S80) shows a highly porous structure. In all other samples (S70 and S60), the addition of PVDF binder changes the appearance of the sample surface, which becomes denser due to the stronger blockage of the pores by the PVDF binder in the S70 and S60 samples. After fully discharging, the structure of the discharged air cathode changed significantly. For the SD85 cathode, the microstructure is characterized by a fragile fractured surface. The grain morphology of the flat areas was also evidenced. In the grain surface, there is a growth of a crust-like layer speculated to be a discharge product of $Al(OH)_3$. This substance is produced during the discharge reaction process and is a nonconductive metallic oxide. The formation mechanism of the $Al(OH)_3$ layer is consistent with the published result in a previous study on an air cathode of activated carbon for an Al air battery cell [30]. For the SD80 cathode, the SEM images exhibit a porous shape with low homogeneity and irregular agglomerates. In some locations, the porous surface is covered by a small amount of the $Al(OH)_3$ layer formed during the discharge process. Furthermore, the SD70 sample contains an increased amount of the $Al(OH)_3$ layer, and in the SD60 sample, more pores are covered by a large amount of $Al(OH)_3$ layer; therefore, the sample surface appears to have a denser layer.
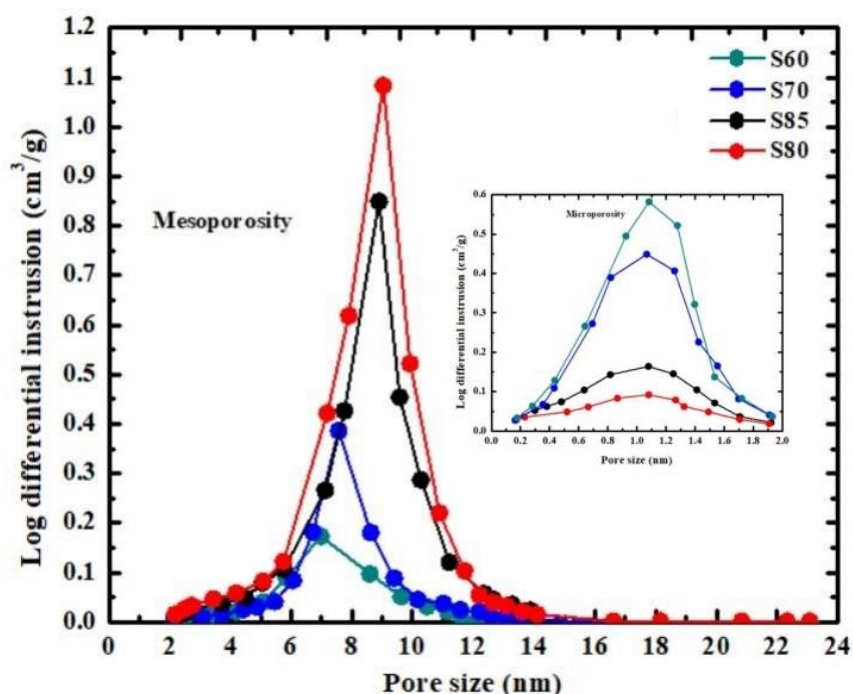

Figure 5. Pore size distributions of the air cathode before discharge.

Figure 5 shows the pore size distribution of the air cathode before discharge. All samples consist of a sharp distribution of micropores with a pore size of less than 2 nm and mesopores with a pore size between 2 nm and 50 nm. The general trend of log differential intrusion in the micropore size range gradually decreases with decreasing PVDF content from 30 wt % (S60) to 10 wt % (S80) and thereafter increases with decreasing PVDF content to 5 wt % (S85). The mesopore size range acts in the opposite direction. Both the increase and decrease in the log differential intrusion are attributed to an increase and

decrease in the volume fraction for the structural pores consisting of isolated and interconnected pores in both micropores and mesopores [31]. For a higher content of PVDF, an increase in the volume fraction of micropores may be attributed to an increase in the blocked mesopores of the air cathode, while a decrease in the volume fraction of mesopores is ascribed to the precipitation of the PVDF/NMP solution, and precipitate phases cause the densified microstructure and the decreased connectivity in the gaps of pore spaces so that they generate a lower total porosity. In this way, the decreased porosity and the increased compactness of the sample are created. Furthermore, in the mesopore size range, the pore size is shown to shift toward a smaller pore size with increasing PVDF content. This shift of pore size is related to at least two facts. First, as PVDF binding increases, more PVDF particles fill the mesopore space. Second, the lower surface tension of the solutions with a higher PVDF content results in a reduction in the size of the pores [32].
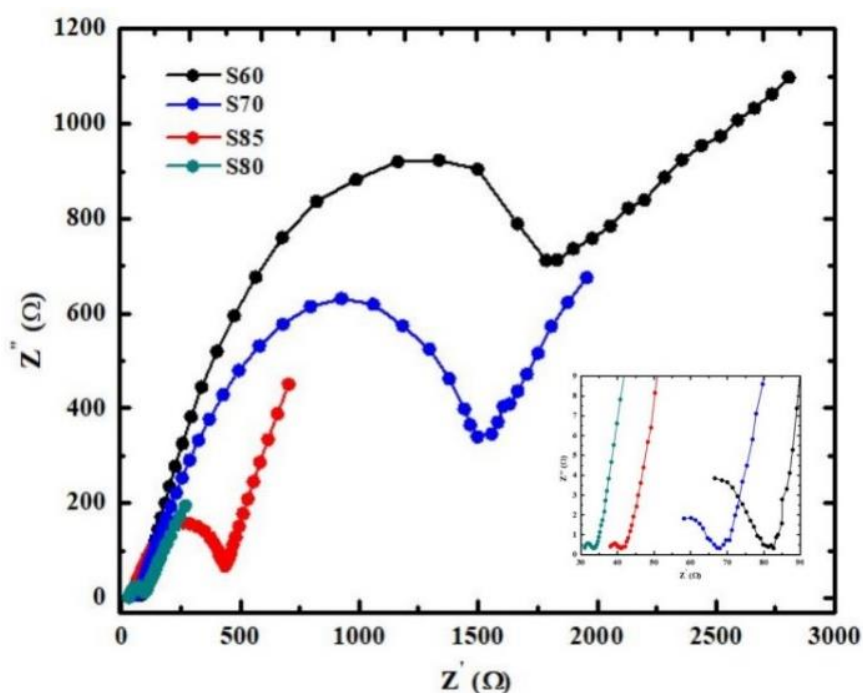
Figure 6. Nyquist plot of EIS spectra for the Al-air batteries using air cathodes with different content of PVDF.

Figure 6 shows the Nyquist plot of the EIS spectra for the Al-air batteries using the air cathode with different PVDF content. For all the samples, the plot consists of an incomplete small semicircle, an out-of-shape large semicircle, and a straight line inclined at an angle to the real axis in the high-, intermediate-, and low-frequency regions (Warburg regions), respectively. A starting point of the small semicircles in the Nyquist plot represents the equivalent series resistance (Rs) associated with the electrolyte solution, current collectors, and contact resistances [33]. As shown in the inset of Figure 6, Rs increases as the PVDF content increases from 5 wt % (S85) to 30 wt % (S60). This behavior is attributed to the formation of reduced interconnection networks between the SX and CB particles in the composite layer due to the gradual blockage of a larger amount of an electronic active layer by the higher content of PVDF particles. The value of R_s is much higher than S80 sample. According to the SEM observed in the case of the SD85 sample, the fragility of the surface was observed, causing damage to

the conducting matrix between the active particles of a-SX and conductive C. The current collector of the nickel mesh loses contact with the air cathode, and as a result, the contact resistance between the active material and the current collector increases. The small incomplete semicircle can be related to the solid electrolyte interphase layer resistance (R_{SEI}). R_{SEI} originates from the resistance of a layer that forms on the interface between the anode and electrolyte. The R_{SEI} increases with increasing PVDF binder content from 5 wt % (S85) to 30 wt % (S60). The higher volume fraction of mesopores easily induces diffusion of electrolyte ions through the pores and produces more reaction product $Al(OH)_3$ in the electrolyte medium. Therefore, the product of this reaction accumulates on the surface of the Al anode, resulting in an increase in the R_{SEI}, which impedes OH- migration to the Al anode in the discharge reaction. This interpretation is in agreement with similar findings of studies on lithium and magnesium-air batteries [34, 35]. The R_{ct} resistance is associated with the existence of an amount of the $Al(OH)_3$ reaction product [34] that enters the pores in the composite layer and is being adsorbed onto their surfaces. The charge-transfer process between the pore surface in the composite layer and the electrolyte solution is interrupted prematurely and leads to changes in the charge transfer resistance. Furthermore, the out-of-shape large semicircle can be associated with the charge transfer resistance of the cathode and electrolyte interface (R_{ct}). The R_{ct} value increases significantly with increasing PVDF binder content from 5 wt % (S85) to 30 wt % (S60). This finding relates to two facts pertinent to the blocking of the micropore entrance by the discharge product and the formation of water molecules in the pore. Micropores are too small to incorporate $Al(OH)_3$, and according to the literature [36], the entrance of the micropores can easily be blocked by $Al(OH)_3$; thus, these pores remain unfilled by oxygen and electrolyte ions. The increase in R_{ct} may be attributed to the volume fraction of micropores increasing when the SX content increases from 5 wt % (S85) to 30 wt % (S60), so that the pore contact area blocked by $Al(OH)_3$ increases, and therefore, the charge transfer resistance R_{ct} increases. Moreover, the change in the distribution of the discharge product in the cathode due to the presence of the water molecules also takes place [29]. As seen in Figures 6 and 3, there is a clear correlation between R_{ct} and the number of water molecules contained in the discharged sample. Therefore, R_{ct} increases due to an increase in the amount of the discharge product formed in the interior of the mesoporous channel when the PVDF content increases from 5 wt % (S85) to 30 wt % (S60). The S80 sample has the smallest value of R_{ct} due to both the smallest amount of microporous structure and smallest number of water molecules bound in the mesoporous structure of the sample. In this case, growth-restricted discharge products were formed at the mesopore channels of the cathode structure. A straight line in the final plot is related to the Walburg resistance (W). The appearance of the resistance is the consequence of the resistive behaviors of the ions penetrating into the air cathode pores [35]. The slope of the line for the S80 sample is greater than the slope of the line for the S60 and S70 samples, indicating that the diffusion of electrolyte ions in the active layer of the S80 sample is faster than in the two samples S60 and S70 due to the development of more mesopores in the air cathode when the PVDF binder content was lowered to 10 wt % (S80).
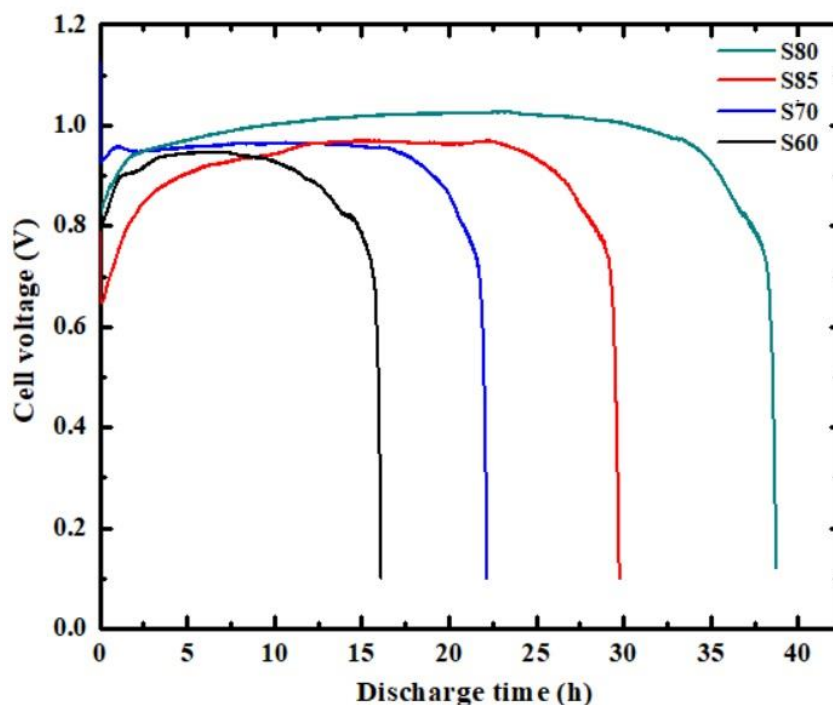
Figure 7. Discharge curve of the Al-air batteries using air cathodes with different PVDF content.

Figure 7 shows the discharge curves of the Al-air battery obtained using air cathodes with different content of PVDF binder. The oven circuit voltage (OCV) of all samples is 1.13 V. At the initial stage of discharging, the voltages of the S85, S80, S70, and S60 samples are observed to drop from the OCV to approximately 0.65 V, 0.82 V, 0.92 V, 0.79 V, respectively. The cause of such a drop in the region may be attributed to insufficient rest time for proper air cathode wetting. In this case, the electrolyte is inserted only into the amorphous surface layer and has not seeped deeply into the interior of mesoporous channels so that it will reduce the electrolyte permeability and cause uneven contact between the electrolyte and active sites of the sample, thus resulting in a voltage drop. Furthermore, the voltage quickly recovers to approximately 0.97 V, 1.02 V, 0.96 V, 0.94 V as a stable plateau voltage, respectively. The batteries maintained a stable voltage to treat the discharge process for 16.84 h, 22.16 h, 38.73 h, and 29.94 h, respectively. A decrease in the stable voltage length is caused by an increase in the content of PVDF binder. According to the EIS results, this decrease is attributed to an increase in the R_{ct} in the active layer of the air cathode due to the blocking of the entrance of the electrolyte into the micropores by discharge products and the formation of discharge products bound in water molecules in the mesopore channels. Such behavior is in line with the interpretations from the related studies on Al-air batteries using iron [36], carbon fiber cloth [37], and carbon composite [38] as an air cathode. Table 2 shows the comparison of SiO_2/C with other materials as air cathodes for primary Al-air batteries. The Al-air battery using the SiO_2/C composite in the present study exhibits a stable voltage of 0.96 V and a discharge time of 38.73 h. These values are similar and are higher than the values obtained for the Al-air battery using the $SiO_2/graphite$ composite as an air cathode. A decrease in discharge time may be attributed to the introduction of graphite as an additive material. During the discharging process, graphite

experiences a larger volume expansion than carbon black [42] so that it creates a larger gap between the graphite particles and contraction of the graphite-connected Si particles by the GG binder. Therefore, both contribute to an increase in the loss of electrochemical activity of the SiO_2/graphite composite electrode. Furthermore, these results also demonstrate that the discharge time of our result is much higher than the discharge time obtained for Al-air batteries with different active materials, viz., MnO_2, carbon and Pt. The reason for this difference in discharge time may be attributed to at least two factors. First, the detailed analysis of these investigations reveals the role of the side reaction [43, 44] and shows that the carbon electrode undergoes the deterioration of the electrochemical reaction due to carbon combustion by active oxygen species during discharging. Second, in the presence of the binder, the MnO_2, carbon and Pt particles in the composite agglomerate strongly during the slurry preparation of the active layer [45-47] so that the microstructure of agglomerated particles has narrow and uneven pores. As a result, the pore utilization can be more limited for both O_2 diffusion and electrolyte access to the air cathode active surface. In contrast, in our study, carbon black and SiO_2 agglomerates were more brittle due to the high porosity of these agglomerates. The microstructure of agglomerated SiO_2 was not as dense as the microstructure in agglomerated carbon and MnO_2 particles. These larger pore channels provide pathways for electrolyte ingress and accommodate the cathode active mass volume expansion during discharging.

Table 2. Comparison of SiO_2/C with other materials as air cathodes for primary Al-air batteries

Air cathode material	Stable plateau voltage (V)	Discharge time (h)	References
SiO_2/graphite	0.98	8.92	[15]
MnO_2/C	0.86	12.72	[39]
Carbon fiber cloth	0.92	1.62	[37]
Ag_2MnO_4/C	0.95	7.49	[40]
Pt/C	0.95	7.34	[41]
SiO_2/C	0.96	38.73	This work

4. CONCLUSIONS

A porous air cathode for treating the first discharge of an Al-air battery has been successfully produced from an amorphous silica xerogel and PVDF as a binder. In the prepared air cathode, the introduction of PVDF for the binder of the active layer affects the formation of a porous structure in the a-SX sample. The microporous structure decreases as the content of PVDF binder decreases from 30 wt % (S60) to 10 wt % (S80) and then increases slightly as the content decreases to 5 wt % (S85), while the mesoporous structure acts in the opposite direction. The presence of the resulting porous structure generates a change in the stable plateau voltage length for the discharge capacity of the Al-air battery. The micropore sizes are too small to incorporate the discharge products of $Al(OH)_3$. The entrance of these micropores can easily be blocked by the $Al(OH)_3$ layer; thus, these pores remain unfilled by oxygen and electrolyte ions; therefore, the larger amount of microporous structures significantly reduces the length of the stable plateau voltage. Furthermore, the number of water molecules bound in the sample changes the discharge product formation from the restricted to easily grown $Al(OH)_3$ layer in the interior

of the mesopore channels, resulting in a significant decrease in the stable plateau voltage. The air cathode of the a-SX sample with a PVDF binder content of 10 wt % delivers the longest stable plateau voltage for 38.73 h.

References

1.   M.C. Gonçalves, *Molecules*, 23(2018)1.
2.   N. P. Shetti, S. J. Malode, D. S. Nayak, K. R. Reddy, C. V. Reddy , and K. Ravindranadh, *Microchem. J.*, 150(2019)104206.
3.   H. Zhang, Z. Zou, S. Zhang, J. Liu, S. Zhong, *Int. J. Electrochem. Sci.*, 15(2020)12041.
4.   M. A. Rahman, X. Wang, and C. Wen, *J. Electrochem. Soc.*, 160(2013)A1759.
5.   C. Wang, Y. Yu, J. Niu, Y. Liu, D. Bridges, X. Liu, J. Pooran, Y. Zhang, and A. Hu, *Appl. Sci.*, 9(2019)1.
6.   I.H. Cho, P.Y. Lee, and J.H. Kim, *Energies (Basel, Switz.)*,12(2019)3023.
7.   H. F. Wang, and Q. Xu, *Matter*, 1(2019)565.
8.   Y. Zhao, Z. Liu, Y. Zhang, A. Mentbayeva, X. Wang, M. Y. Maximov, B. Liu, Z. Bakenov, and F. Yin, *Nanoscale Res. Lett.*,12(2017)459.
9.   X. Cai, L. Lai, J. Lin, and Z. Shen, *Mater. Horiz.*, 4(2017)945.
10.   V. Roev, S. B. Ma, D. J. Lee, and D. Im, *J. Electrochem. Sci. Technol.*, 5(2014)58.
11.   M. N. Obrovac, *Curr. Opin. Electrochem.*, 9(2018)8.
12.   A. A. Aboalhassan, , J. Yan, Y. Zhao, K. Dong, X. Wang, J. Yu, and B. Ding, *iScience*, 16(2019)122.
13.   W. Li, B. Song, and A. Manthiram, *Chem. Soc. Rev.*, 46(2017)3006.
14.   E. Guerrini, M. Grattieri, A. Faggianelli, P. Cristiani, and S. Trasatti, *Bioelectrochem*istry, 106(2015)240.
15.   H. Aripin, N. Hiron, N. Busaeri, F. Nursuwars, L. Faridah, and S. Sabchevski, *IEEE Int. Conf. on Sustainable Engineering and Creative Computing*, (2020)136.
16.   H. Aripin, S. Mitsudo, I.N. Sudiana, S. Tani, K. Sako, Y. Fujii, T. Saito, T. Idehara, and S. Sabchevski, *J. Infrared, Millimeter, Terahertz Waves*, 32(2011)867.
17.   H. Aripin, S. Mitsudo, I.N. Sudiana, T. Saito, and S. Sabchevski, *Trans. Indian Ceram. Soc.*, 74 (2015)1.
18.   Y. Li, and S. Chin Tjong, *Curr. Nanosci.*, 8(2012)732.
19.   Y. Yu, M. Chen, S. Wang, C. Hill, P. Joshi, T. Kuruganti, and A. Hu, *J. Electrochem. Soc.*, 165(2018)A584.
20.   X. Zhao, Y. Wang, J. Luo, P. Wang, P. Xiao, and B. Jiang, *Silicon*, 13(2021)3413.
21.   H. Mei, Y. Yang, A. C. T. van Duin, S. B. Sinnott, J. C. Mauro, L. Liu, and Z. Fu, *Acta Mater.*, 178(2019)36.
22.   M. H. Shahrokh Abadi, A. Delbari, Z. Fakoor, and J. Baedi, *J. Ceram. Sci. Technol.*, 6(2015)41.
23.   A. Oufakir, L. Khouchaf, M. Elaatmani, A. Zegzouti, G. Louarn, and A. Ben Fraj, *MATEC Web Conf.*, 149(2018)1.
24.   H. Widiyandari, P. Pardoyo, J. Sartika, O. A. Putra, A. Purwanto, and L. Ernawati, *Int. J. Eng., Trans. A*, 34(2021)1569.
25.   Y. Xia, J. Li, H. Wang, Z. Ye, X. Zhou, H. Huang, Y. Gan, C. Liang, J. Zhang, and W. Zhang, *J.

       *Solid State Electrochem.***,** 23(2019)519.

26.   O. H. Teresa, and C. K Choi, *J. Korean Phys. Soc.*, 56(2010)1150.
27.   H. Te Teng , T. Y. Lee, Y. K. Chen, H. W. Wang, and G. Cao, *J. Power Sources*, 219(2012)16.
28.   W. H. Lee, S. R. Choi, and J. G. Kim, *ACS Omega*, 6(2021)25529.
29.   M. Kim, H. Lee, H. Kwon, S.-M. Bak, C. Jaye, D. Fischer, G. Yoon, J. Park, D.-H. Seo, S. Ma, and D. Im, *Sci. Adv.*, 8(2022)1.
30.   R. Mori, *Sustainable Energy Fuels*, 1(2017)1082.
31.   H. Aripin, E. Priatna, D. Dedi, I.N. Sudiana, and S. Sabchevski, *Int. J. Eng., Trans. B*, 35(2022)300.
32.   Z. Yu, and G. Ye, *Constr. Build. Mater.*, 45(2013)30.
33.   N. A. Salleh, S. Kheawhom, and A. A. Mohamad, *Arabian J. Chem.*, 13(2020)6838.
34.   S. Y. Liew, J. C. Juan, C. W. Lai, G. T. Pan, T. C. K. Yang, and T. K Lee, *Ionics*, 25(2019)1291.
35.   H. Kitaura, and H. Zhou, *Adv. Energy Mater.*, 2(2012)889.
36.   H. Cao, S. Si, X. Xu, J. Li, C. Lan, *Int. J. Electrochem. Sci.*, 14(2019) 9796.
37.   W. C. Tan, L. H. Saw, M. C. Yew, D. Sun, Z. Cai, W. T. Chong, and P.-Y. Kuo, *Front. Energy Res.*, 9(2021)1.
38.   S. Choi, D. Lee, G. Kim, Y. Y. Lee, B. Kim, J. Moon, and W. Shim, *Adv. Funct. Mater.,* 27(2017)1.
39.   P. Teabnamang, W. Kao-Ian, M. Nguyen, T. Yonezawa, R. Cheacharoen and S. Kheawhom, *Energies (Basel, Switz.)*, 13(2020) 2275.
40.   J. Ryu, H. Jang, J. Park,Y. Yoo, M. Park, and J. Cho, *Nat. Commun.*, 9(2018)3715.
41.   Y. Yu, M. Chen, S. Wang, C. Hill, P. Joshi, T. Kuruganti, and A. Hu, *J. Electrochem. Soc.*, 165(2018)A1.
42.   S. Priyono, T. D. Sari, R. Ramlan, A. Subhan and B. Prihandoko, *J. Phys.: Conf. Ser.*, 1282(2019)012056.
43.   Z. Xia, Y. Zhu, W. Zhang, T. Hua, T. Chen, J. Zhang, Y. Liu, H. Ma, H. Fang, L. Li, *J. Alloys Compd.*, 824(2020)153950.
44.   T. Guo, X. Qin, X. Gao, L. Hou, J. Li, X. Li, T. Lei and J. Lv, *Fullerenes, Nanotubes, Carbon Nanostruct.*, 27(2019)299.
45.   A. Sumboja, X. Ge, G. Zheng, F. W. T. Goh, T. S. A. Hor, Y. Zong, Z. Liu, *J. Power Sources*, 332(2016)330.
46.   K. Li, X. Liu, *J. Power Sources*, 264(2014)248.
47.   P. Herves, M. Perez-Lorenzo, L. M. Liz-Marzan, J. Dzubiella, Y. Lu, M. Ballauff, *Chem. Soc. Rev.*, 41(2012)5577.